



Regulating the coordination environment of Co single atoms for achieving efficient electrocatalytic activity in CO₂ reduction

Zhigang Geng^{a,1}, Yuanjie Cao^{b,1}, Wenxing Chen^c, Xiangdong Kong^a, Yan Liu^a, Tao Yao^{b,*}, Yue Lin^{a,*}

^a Hefei National Laboratory for Physical Sciences at the Microscale, University of Science and Technology of China, Hefei, Anhui 230026, PR China

^b National Synchrotron Radiation Laboratory, University of Science and Technology of China, Hefei, Anhui 230029, PR China

^c Department of Chemistry, Tsinghua University, Beijing 100084, PR China

ARTICLE INFO

Keywords:

Co single-atom catalysts
N coordinated environment
CO₂ electrochemical reduction

ABSTRACT

Regulating the coordination environment of Co single-atom catalysts represents a powerful strategy to enhance its catalytic performance for CO₂ electrochemical reduction. Herein, we adopt metal-organic frameworks (MOFs) to assist the preparation of Co single-atom catalysts with four-coordinated N and four-coordinated N/C on N-doped porous carbon. The atomic dispersion of Co atoms species on the N-doped porous carbon were confirmed using high-angle annular dark-field scanning transmission electron microscopy (HAADF-STEM) and X-ray absorption fine structure (XAFS) analysis. XAFS results revealed that the coordination number of the N binding to the Co single atom was strongly dependent on the pyrolysis temperature. The Co atoms with four-coordinated N on N-doped porous carbon (Co₁-N₄) exhibited a Faradaic efficiency of 82% and a current density of -15.8 mA cm⁻² for CO production in CO₂ electrochemical reduction. Moreover, the Co₁-N₄ catalytic site also held remarkable stability for 10-hour potentiostatic test towards CO₂ electrochemical reduction. Mechanistic study further revealed that the Co₁-N₄ active site promotes the binding strength of CO₂ and facilitates CO₂ activation, which was responsible for its excellent CO₂ electrochemical reduction performance.

1. Introduction

Owing to the increased concentration of atmospheric CO₂ and the limited reservoir of fossil fuels, there is an urgent need to design robust and efficient catalysts to convert greenhouse CO₂ into valuable chemicals [1–7]. Electrochemical reduction of CO₂ into value-added products is an effective approach to mitigate the environment and energy issues [8–15]. At present, the bottleneck of CO₂ electrochemical reduction is the large overpotential for electron transfer from the catalysts to CO₂ and multiple distribution of products derived from competitive side reactions such as the hydrogen evolution reaction (HER) [16–24]. As a result, rational design of highly active and selective catalysts is important to make practical CO₂ electrochemical reduction in a reality.

Single-atom catalysts have drawn worldwide attention for many electrochemical transformation processes with remarkable catalytic activity due to the high ratio of unsaturated coordinated and maximum utility of atoms [25–28]. Moreover, the coordination environment for single-atom catalysts is also an important factor to regulate the catalytic activity and selectivity. For instance, Co single atoms dispersed on N-

doped graphene exhibited more excellent HER activity with an onset potential of ~30 mV than that of the Co single atoms dispersed on graphene, owing to the high-temperature-induced strong coordination between the Co and N [29]. In addition, Fe-N_x species atomically dispersed on the N and S co-decorated hierarchical carbon layers was proven to be a state-of-the-art oxygen reduction reaction catalyst, since the positively charged carbon atoms favor adsorption of oxygen species by inducing uneven charge distribution in the carbon framework [30]. Most of the reported studies have theoretically proved that the different coordination environment influenced the catalytic activity of the single-atom catalysts for electrochemical transformation process [31,32]. However, to the best of our knowledge, the regulation of the coordination environment of single-atom catalysts towards CO₂ electrochemical reduction has seldom been studied.

Herein, we adopt metal-organic frameworks (MOFs) to assist the preparation of Co single-atom catalysts with four-coordinated N and four-coordinated N/C on N-doped carbon under different pyrolysis temperature. During CO₂ electrochemical reduction process, the Co atoms with four-coordinated N on N-doped carbon (Co₁-N₄) exhibited

* Corresponding authors.

E-mail addresses: yaot@ustc.edu.cn (T. Yao), linyue@ustc.edu.cn (Y. Lin).

¹ These authors contributed equally to this work.

higher catalytic activity than that of the Co single atoms with four-coordinated N/C dispersed on the N-doped carbon (Co₁-N_{4-x}C_x), with a Faradaic efficiency (FE) of 82% and a current density of -15.8 mA cm⁻² for CO production. Mechanistic study further revealed that the higher catalytic performance of Co₁-N₄ relative to that of Co₁-N_{4-x}C_x originated from the promoted binding strength of CO₂ and the facilitated CO₂ activation, due to the difference of the coordination environment with central Co active site.

2. Experimental

2.1. Synthesis of Co₁-N₄ and Co₁-N_{4-x}C_x

A mixture of Zn(NO₃)₂·6H₂O (1.630 g) and Co(NO₃)₂·6H₂O (0.051 g) was dissolved in 80 mL of methanol, which was subsequently added into 80 mL of methanol containing 3.7 g of 2-methylimidazole (MeIM). Then the mix solution was kept at 25 °C for 12 h. The as-obtained blue precipitates were centrifuged and washed with methanol for five times, and finally dried at 65 °C under vacuum for overnight. The as-obtained blue precipitates were denoted as ZnCo bimetallic MOF. Next, ZnCo bimetallic MOF was heated to 800 °C with a heating rate of 5 °C min⁻¹ in a tube furnace, and kept at 800 °C under flowing N₂ gas for 3 h. After the tube furnace was naturally cooled to room temperature, the Co₁-N₄ catalyst was obtained and directly used as the catalyst without further treatment. The Co₁-N_{4-x}C_x was prepared *via* the similar synthetic procedure with that of Co₁-N₄ except that the heated temperature was set to 900 °C.

2.2. Synthesis of ZIF-8-800 and ZIF-8-900

In a typical procedure, 1.681 g of Zn(NO₃)₂·6H₂O was dissolved in 80 mL of methanol, which was subsequently added into 80 mL of methanol containing 3.7 g of 2-MeIM. Then the mixed solution was kept at 25 °C for 12 h. The as-obtained precipitate was separated by centrifugation and washed subsequently with methanol for five times. Finally, the ZIF-8 was obtained by being dried at 65 °C under vacuum for overnight. Next, the ZIF-8 was heated to 800 °C with a heating rate of 5 °C min⁻¹ in a tube furnace, and kept at 800 °C under N₂ flow for 3 h. After the tube furnace was naturally cooled to room temperature, the ZIF-8-800 was obtained and directly used as the catalyst without further treatment. ZIF-8-900 was prepared *via* the similar synthetic procedure with that of ZIF-8-800 except that the heated temperature was set to 900 °C.

2.3. Electrochemical measurements

Electrochemical measurements were performed in a three-electrode system at an electrochemical station (CHI660E). Typically, 1.0 mg of the as-prepared catalysts and 15 µL of Nafion solution (5 wt%) were dispersed in 1 mL of ethanol by sonication for 1 h. The dispersion was then uniformly spread on carbon fiber paper with an area of 1 × 0.5 cm². The prepared electrodes as the working electrode were dried overnight under vacuum for further use. In CO₂ electrochemical reduction, the electrochemical measurements were carried out in an H-cell system which was separated by Nafion 115 membrane. The graphite rod and Ag/AgCl electrodes were used as the counter electrode and reference electrode, respectively. The potentials were controlled by an Autolab potentiostat/galvanostat (CHI660E). All potentials in this study were measured against the Ag/AgCl reference electrode and converted to the RHE reference scale based on the following equation: E (vs RHE) = E (vs Ag/AgCl) + 0.21 V + 0.0591 × pH. Linear sweep voltammograms (LSV) curves of the catalysts were performed in CO₂-saturated and Ar-saturated 0.1 M KHCO₃ (pH = 6.8) with the scan rate of 5 mV s⁻¹. Electrochemical reduction of CO₂ was conducted in CO₂-saturated 0.1 M KHCO₃ solution under atmospheric pressure at room temperature. After CO₂ was purged into the 0.1 M KHCO₃ solution for

at least 30 min to remove residual air, controlled potential electrolysis was performed at each potential for 40 min. The gas products of CO₂ electrochemical reduction were monitored by an online Gas Chromatography (GC) equipped with a Thermal Conductivity Detector (TCD) and Molsieve 5A column once every five minutes. For the measurement of liquid products, 0.5 mL of KHCO₃ solution after electrolysis was mixed with 0.1 mL of Deuterium oxide (D₂O). Then 0.1 mL of 6 mM 1-Propanesulfonic acid 3-(trimethylsilyl) sodium salt (DSS) solution was added as an internal standard. The ¹H nuclear magnetic resonance (NMR) spectrum was measured on a Varian 400 MHz NMR spectrometer. No liquid products have been detected in this case. The cyclic voltammetry measurement was conducted in 0.1 M KHCO₃ solution using three-electrode cell equipped with a Ag/AgCl reference electrode and a graphite rod counter electrode at 25 °C. Cyclic voltammogram measurements of Co₁-N₄ and Co₁-N_{4-x}C_x were conducted from 0.64 to 0.74 V vs RHE and 0.65 to 0.75 V vs RHE with various scan rates (1, 5, 10, 20, and 30 mV s⁻¹) under CO₂ atmosphere to obtain the double layer capacitance (*C*_{dl}). The *C*_{dl} for Co₁-N₄ and Co₁-N_{4-x}C_x was estimated by plotting the Δj (*j*_a - *j*_c) at 0.69 and 0.70 V vs RHE against the scan rates, in which *j*_a and *j*_c were the anodic and cathodic current density, respectively [33,34]. The linear slope was equivalent to twice of the *C*_{dl}. The electrochemical surface areas (ECSAs) were calculated by the following equation: ECSAs = *R*_f*S*, where *R*_f represented the roughness factor of Co₁-N₄ and Co₁-N_{4-x}C_x, *S* represented the surface area of the carbon paper electrode. The value of *R*_f was positively correlated with the *C*_{dl}.

2.4. Instruments

Transmission electron microscopy (TEM) images were taken using a Hitachi H-7650 transmission electron microscope at an acceleration voltage of 100 kV. High-angle annular dark field scanning transmission electron microscopy (HAADF-STEM) images were carried out on a JEOL ARM-200F field-emission transmission electron microscope operating at an accelerating voltage of 200 kV using Cu-based TEM grids. X-ray photoelectron spectroscopy (XPS) measurements were performed on a VG ESCALAB MK II X-ray photoelectron spectrometer with an exciting source of Mg Kα = 1253.6 eV. The gas products of CO₂ electrochemical reduction were monitored by an online GC (SHIMADZU, GC-2014) equipped with a TCD detector and Molsieve 5A column. The liquid products in CO₂ electrochemical reduction were examined on a Varian 400 MHz NMR spectrometer (Bruker AVANCE AV III 400). Inductively coupled plasma-atomic emission spectroscopy (ICP-AES) (Atomscan Advantage, Thermo Jarrell Ash, USA) was used to determine the concentration of Co species. CO₂ temperature-programmed desorption (CO₂-TPD) profiles were recorded by micromeritics AutoChem II 2920 chemisorption analyzer. X-ray absorption fine structure (XAFS) spectra at the Co K-edge (7709 eV) were measured at the 1W1B beamline of Beijing Synchrotron Radiation Facility (BSRF) in China. The output beam was selected by Si (111) monochromator. The dates were collected at room temperature under fluorescence mode by using solid state detector. Diffuse reflectance infrared fourier transform spectroscopy (DRIFTS) experiments were conducted in an elevated-pressure cell (DiffusIR Accessory PN 041-10XX) with a Fourier transform infrared spectrometer (TENSOR II Sample Compartment RT-DLaTGS).

3. Results and discussion

3.1. Material analysis

Typically, Co₁-N₄ and Co₁-N_{4-x}C_x were prepared *via* pyrolyzing the ZnCo bimetallic MOF at 800 °C and 900 °C, respectively. The ZnCo bimetallic MOF were synthesized through the standard synthetic route of zeolitic imidazolate frameworks (ZIF-8) except for partial substitution of Zn(NO₃)₂ with Co(NO₃)₂ [35,36]. Owing to the same coordination of Co²⁺ and Zn²⁺ with 2-MeIM, the intentional addition of Co²⁺ replaced

a certain proportion of Zn^{2+} sites and further expanded the adjacent distances of Co atoms. The spatial interval between two Co atoms was finely controlled, which was beneficial to form the Co single atoms during the pyrolysis process. In addition, in the ZnCo bimetallic MOF, the Co^{2+} and Zn^{2+} was coordinated with 2-MeIM by four nitrogen atoms, which further provided a requirement for preparing the Co single atoms with different coordination environment under different pyrolysis temperature. As shown by TEM images in Fig. S1, the ZnCo bimetallic MOF exhibited the same morphology of homogeneous rhombododecahedron and an average size about 60 nm as ZIF-8. After the pyrolysis process, no peaks at 1022 eV were observed in the XPS spectra of $\text{Co}_1\text{-N}_4$ and $\text{Co}_1\text{-N}_{4-x}\text{C}_x$, demonstrating that Zn^{2+} species in ZnCo bimetallic MOF has been evaporated (Fig. S2). Meanwhile, the characteristic peaks at 285 eV, 401 eV, and 530 eV corresponded to C 2p, N 1s, and O 2p respectively, which indicated that organic linker in ZnCo bimetallic MOF were transformed into N-doped carbon. The loading amount of Co in $\text{Co}_1\text{-N}_4$ and $\text{Co}_1\text{-N}_{4-x}\text{C}_x$ were determined to be 0.60% and 0.63% by ICP-AES, respectively. As shown in the TEM images of $\text{Co}_1\text{-N}_4$ and $\text{Co}_1\text{-N}_{4-x}\text{C}_x$, the original structure shrank into porous irregular rhombododecahedrons with an average size of 50 nm after pyrolysis process (Figs. 1a and S3a). According to the ring-like selected-area electron diffraction pattern taken from individual $\text{Co}_1\text{-N}_4$ and $\text{Co}_1\text{-N}_{4-x}\text{C}_x$ rhombododecahedron (Figs. 1b and S3b), both $\text{Co}_1\text{-N}_4$ and $\text{Co}_1\text{-N}_{4-x}\text{C}_x$ exhibited a poor crystallinity (Figs. 1c and S3c). The HAADF-STEM images of $\text{Co}_1\text{-N}_4$ and $\text{Co}_1\text{-N}_{4-x}\text{C}_x$ demonstrated that individual Co atoms were uniformly dispersed (Figs. 1d, 1e, S3d, and S3e). The HAADF-STEM images and the energy-dispersive X-ray spectroscopy (EDS) elemental mapping analysis for $\text{Co}_1\text{-N}_4$ and $\text{Co}_1\text{-N}_{4-x}\text{C}_x$ further revealed the C, N, and Co elements uniformly dispersed over the whole structures (Figs. 1f and S3f).

To further explore the coordination environment of the $\text{Co}_1\text{-N}_4$ and $\text{Co}_1\text{-N}_{4-x}\text{C}_x$, we performed the XAFS measurements. As shown in the X-ray absorption near-edge structure (XANES) spectra at the Co K-edge (Fig. 2a), the energy absorption threshold value for $\text{Co}_1\text{-N}_4$ was higher than that of Co foil, and between that of CoO and Co_3O_4 , indicating that the Co species in $\text{Co}_1\text{-N}_4$ was the ionic state (close to Co^{2+} or Co^{3+}). In addition, the energy absorption threshold value of $\text{Co}_1\text{-N}_{4-x}\text{C}_x$ was much closer to $\text{Co}_1\text{-N}_4$, which revealed that the valence state of Co species in

$\text{Co}_1\text{-N}_{4-x}\text{C}_x$ was the same as that in $\text{Co}_1\text{-N}_4$. Furthermore, more structural information about Co single atoms was obtained by the extended X-ray absorption fine structure (EXAFS). Fig. 2b showed the Fourier transformed k^3 -weighted $\chi(k)$ function of the EXAFS spectra for $\text{Co}_1\text{-N}_4$, $\text{Co}_1\text{-N}_{4-x}\text{C}_x$, and Co foil. The main peak for $\text{Co}_1\text{-N}_4$ and $\text{Co}_1\text{-N}_{4-x}\text{C}_x$ appeared at ca. 1.35 Å, which was ascribed to Co-N/Co-C coordination peak. Together with the absence of the Co-Co path at 2.16 Å, it was confirmed that Co in the $\text{Co}_1\text{-N}_4$ and $\text{Co}_1\text{-N}_{4-x}\text{C}_x$ exhibited in the form of single atomic dispersion. According to the EXAFS fitting results (Table S1), the total coordination number of the first Co-N plus Co-C shell for the Co atom in $\text{Co}_1\text{-N}_4$ and $\text{Co}_1\text{-N}_{4-x}\text{C}_x$ was approximate four (Figs. 2c and S4). Considering the difficulties in discriminating the C/O neighbors by EXAFS, we resort to EXAFS wavelet transform (WT) analysis that is powerful for discriminating the backscattering atoms even when they overlap substantially in R-space, providing not only radial distance resolution but also k-space resolution [37]. As shown in Fig. 2d, the WT contour maximum at 4.3 Å⁻¹ for $\text{Co}_1\text{-N}_4$ and 4.0 Å⁻¹ for $\text{Co}_1\text{-N}_{4-x}\text{C}_x$ confirmed the presence of Co-N(C) bonding. The difference of ~0.3 Å⁻¹ between the maximum for $\text{Co}_1\text{-N}_{4-x}\text{C}_x$ (4.0 Å⁻¹) and $\text{Co}_1\text{-N}_4$ (4.3 Å⁻¹) might arise from the shorter Co-C path. Meanwhile, no intensity maximum corresponding to Co-Co was observed, compared with the WT contour plots of Co foil, Co_3O_4 , and CoO (Fig. S5). Based on the XAFS analysis, we considered that the Co-C coordination took place of the partial Co-N coordination under high pyrolysis temperature for $\text{Co}_1\text{-N}_{4-x}\text{C}_x$.

3.2. Electrochemical characterizations

The two as-prepared Co single-atom catalysts were applied in CO_2 electrochemical reduction reaction. LSV curves for $\text{Co}_1\text{-N}_4$ and $\text{Co}_1\text{-N}_{4-x}\text{C}_x$ were performed in CO_2 -saturated and Ar-saturated 0.1 M KHCO_3 electrolyte from 0 to -1.0 V vs RHE (Figs. 3a and S6), respectively. Both $\text{Co}_1\text{-N}_4$ and $\text{Co}_1\text{-N}_{4-x}\text{C}_x$ exhibited higher current density in CO_2 -saturated electrolyte than that in Ar-saturated electrolyte, demonstrating that CO_2 was electrochemically reduced by these two catalysts. The catalytic performance of $\text{Co}_1\text{-N}_4$ and $\text{Co}_1\text{-N}_{4-x}\text{C}_x$ were further investigated at different applied potential by chrono-amperometry electrolysis. The products for CO_2 electrochemical reduction over $\text{Co}_1\text{-N}_4$ and $\text{Co}_1\text{-N}_{4-x}\text{C}_x$ were determined by GC and ^1H NMR. As shown in

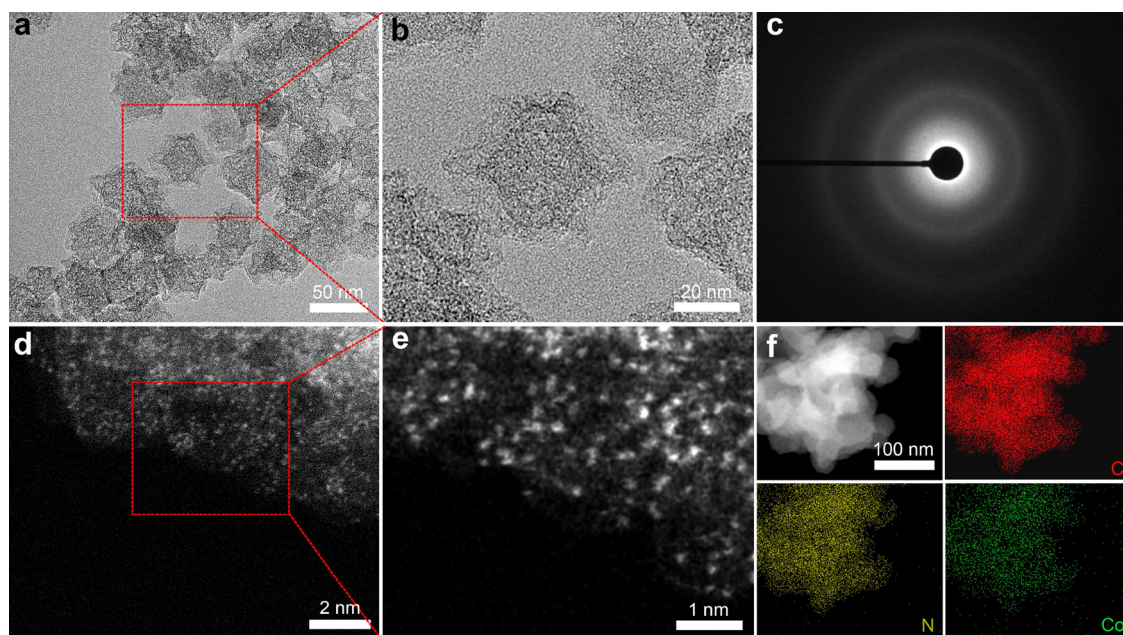


Fig. 1. (a) A typical TEM image and (b) HRTEM image of the $\text{Co}_1\text{-N}_4$. (c) The ring-like selected-area electron diffraction pattern taken from individual $\text{Co}_1\text{-N}_4$. (d) HAADF-STEM image and (e) magnified HAADF-STEM image of $\text{Co}_1\text{-N}_4$. (f) HAADF-STEM image and EDS maps of $\text{Co}_1\text{-N}_4$ revealed the homogeneous distribution of C (red), N (yellow), and Co (green), respectively.

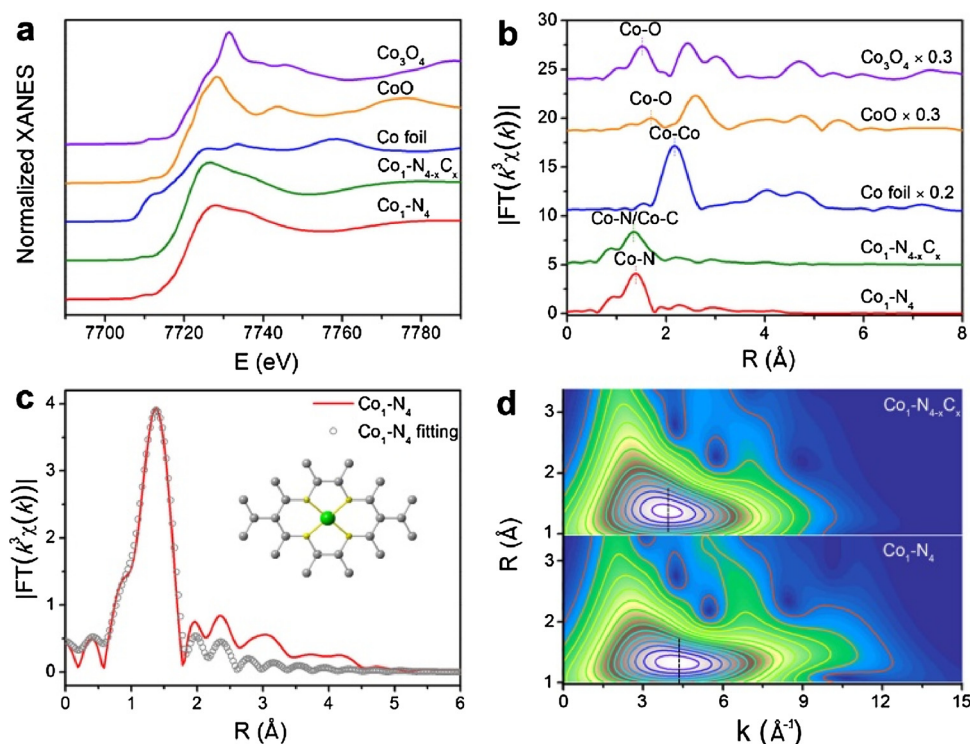


Fig. 2. (a) Co K-edge XANES spectra and (b) Fourier transformed k^3 -weighted $\chi(k)$ function of the EXAFS spectra for $\text{Co}_1\text{-N}_4$, $\text{Co}_1\text{-N}_{4-x}\text{C}_x$, CoO , Co_3O_4 , and Co foil. (c) Fitting results of the EXAFS spectra for $\text{Co}_1\text{-N}_4$ and its atomic structure as inset. The gray, yellow, and green spheres represent C, N, and Co atoms, respectively. (d) WT of the Co K-edge for $\text{Co}_1\text{-N}_{4-x}\text{C}_x$ and $\text{Co}_1\text{-N}_4$.

Fig. 3b, the $\text{Co}_1\text{-N}_4$ exhibited a higher FE for CO production with respect to the $\text{Co}_1\text{-N}_{4-x}\text{C}_x$ at each applied potential. Specifically, when the potential was set at -0.8 V vs RHE, the FE of $\text{Co}_1\text{-N}_4$ for CO production reached up to 82%, whereas the FE of $\text{Co}_1\text{-N}_{4-x}\text{C}_x$ was only 47%. Fig. S7 showed the total FE calculated by summing FE for CO and H_2 production on the $\text{Co}_1\text{-N}_4$ and $\text{Co}_1\text{-N}_{4-x}\text{C}_x$. The total FE for the two catalysts approximately equaled to around 100%, demonstrating no other product during the whole electrochemical reduction process. This result was also consistent with ^1H NMR detection. Fig. 3c showed the current

density for CO production of the $\text{Co}_1\text{-N}_4$ and $\text{Co}_1\text{-N}_{4-x}\text{C}_x$. At each potential, $\text{Co}_1\text{-N}_4$ exhibited a higher current density than that of $\text{Co}_1\text{-N}_{4-x}\text{C}_x$ towards CO_2 electrochemical reduction to CO production. Typically, at -1.0 V vs RHE, the current density of $\text{Co}_1\text{-N}_4$ for CO production was up to -15.8 mA cm^{-2} , which was 1.8 times as high as that of $\text{Co}_1\text{-N}_{4-x}\text{C}_x$. The catalytic performance of $\text{Co}_1\text{-N}_4$ was comparable to that of the state-of-the-art catalysts for electrochemical reduction CO_2 into CO production (Table S2). We further calculated the turnover frequency (TOF) numbers of $\text{Co}_1\text{-N}_4$ and $\text{Co}_1\text{-N}_{4-x}\text{C}_x$ based on the loading amount

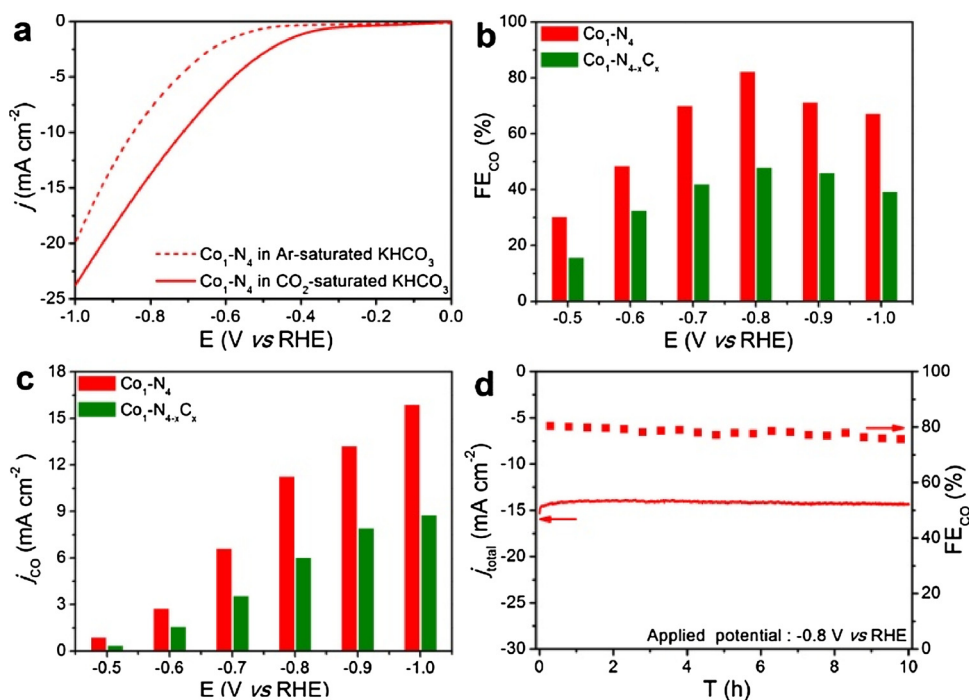


Fig. 3. (a) LSV curves of $\text{Co}_1\text{-N}_4$ were performed in CO_2 -saturated and Ar -saturated 0.1 M KHCO_3 ($\text{pH} = 6.8$). (b) FE and (c) Current density for CO production at selected potentials on $\text{Co}_1\text{-N}_4$ and $\text{Co}_1\text{-N}_{4-x}\text{C}_x$. (d) 10-hour potentiostatic test for $\text{Co}_1\text{-N}_4$ at -0.8 V vs RHE.

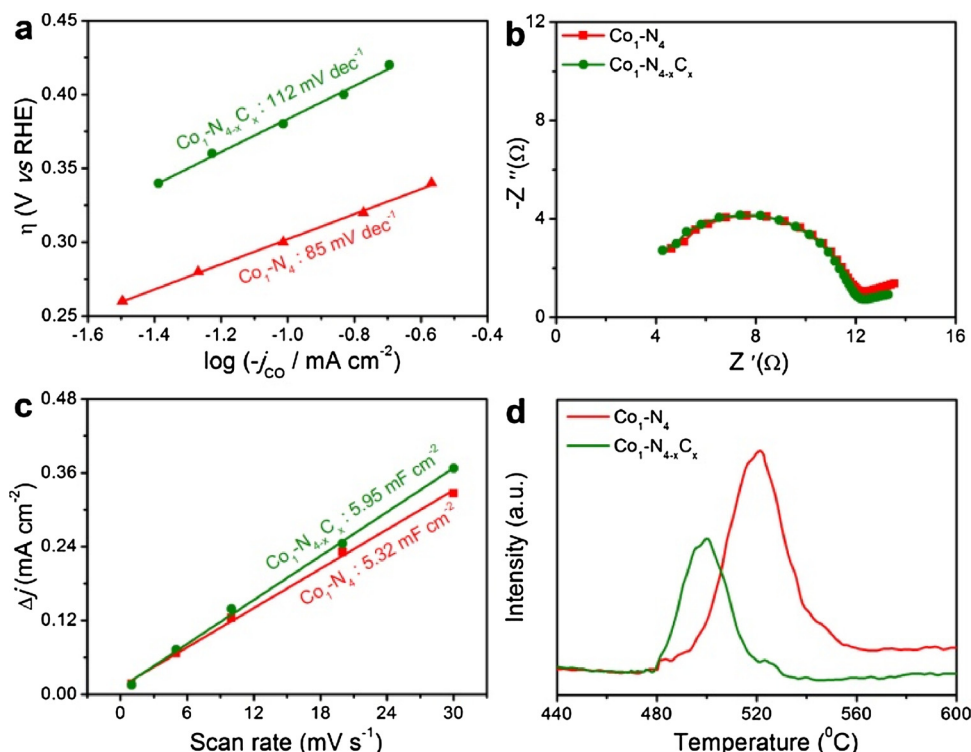


Fig. 4. (a) Tafel plots of CO production for Co₁-N₄ and Co₁-N_{4-x}C_x, (b) Nyquist plots, and (c) Charging current density differences plotted against scan rates were performed in CO₂-saturated 0.1 M KHCO₃ (pH = 6.8). (d) CO₂-TPD profiles for Co₁-N₄ and Co₁-N_{4-x}C_x.

of Co atoms (Fig. S8). Notably, the TOF number of Co₁-N₄ was 1455 h⁻¹, which was about twice as large as that (763 h⁻¹) of Co₁-N_{4-x}C_x at -1.0 V vs RHE. In addition, it was noticeable that another crucial factor for the CO₂ electrochemical reduction performance was the durability. Both the Co₁-N₄ and Co₁-N_{4-x}C_x showed less than 3% decay in current density and 6% decay for FE after a 10-hour potentiostatic test, indicated the preferable durability of the two catalysts (Figs. 3d and S9). After the electrolysis, the Co single atoms were still atomically dispersed on the nitrogen-doped carbon (Fig. S10).

To exclude the influence of the substrate of the N-doped carbon for CO₂ electrochemical reduction, we conducted the substrate of pyrolyzed ZIF-8 at 800 °C (ZIF-8-800) and 900 °C (ZIF-8-900) as catalysts. As shown in Fig. S11, Raman spectra for Co₁-N₄, Co₁-N_{4-x}C_x, ZIF-8-800, and ZIF-8-900 also exhibited the two peaks at 1350 cm⁻¹ and 1580 cm⁻¹, which represented D band and G band of graphite carbon, respectively [38,39]. The intensity ratio of D band to G band (I_D/I_G) for Co₁-N₄, Co₁-N_{4-x}C_x, ZIF-8-800, and ZIF-8-900 were shown in the Fig. S12. The I_D/I_G of Co₁-N₄ was 1.02, close to that of ZIF-8-800, which was higher than that of Co₁-N_{4-x}C_x (0.92) and ZIF-8-900 (0.91). In N 1s spectra of Co₁-N₄, Co₁-N_{4-x}C_x, ZIF-8-800, and ZIF-8-900, three peaks at 398.6 eV, 400.0 eV, and 401.0 eV were assigned to pyridinic N, pyrrolic N, and graphitic N, respectively (Fig. S13) [40,41]. Accordingly, the frame of porous carbon in all of samples possessed the similar degree of disorder for sp² C and N relative with the pyrolysis temperature. The catalytic activities of ZIF-8-800 and ZIF-8-900 for CO₂ electrochemical reduction were evaluated by LSV in CO₂-saturated and Ar-saturated 0.1 M KHCO₃ electrolyte from 0 to -1.0 V vs RHE (Fig. S14). Both ZIF-8-800 and ZIF-8-900 showed a minimal current response, revealing the poor catalytic activity for ZIF-8-800 and ZIF-8-900 towards CO₂ electrochemical reduction. In addition, the FE for H₂ production exceeded 90% for ZIF-8-800 and ZIF-8-900 at all applied potentials (Fig. S15). This result indicated that the catalytic activity of Co single-atom catalysts for CO₂ electrochemical reduction was independent of N-doped carbon frame.

3.3. Mechanistic study

To gain further insights into the reaction kinetics on the Co₁-N₄ and Co₁-N_{4-x}C_x for CO₂ electrochemical reduction into CO production, we analyzed the Tafel plots and electrochemical impedance spectroscopy (EIS). The rate-limiting step of the electrocatalytic reaction was usually determined by the Tafel plots. The whole reaction for CO₂ electrochemical reduction contains three processes (activation process, surface reaction, and desorption process) [42,43]. The Tafel slopes of activation process and surface reaction were theoretically calculated to be approximately 118 mV dec⁻¹ and 59 mV dec⁻¹, respectively [44,45]. In contrast, desorption process did not follow an exponential trend of the current density against potential. As shown in Fig. 4a, the Tafel slopes of Co₁-N₄ and Co₁-N_{4-x}C_x were 85 mV dec⁻¹ and 112 mV dec⁻¹, respectively. As such, the initial CO₂ activation process served as the rate-limiting step for Co₁-N_{4-x}C_x. As for Co₁-N₄, the rate-limiting step was determined by the surface reaction. Based on these results, Co₁-N₄ was found to manipulate the kinetics of CO₂ electrochemical reduction and promote the kinetics of CO₂ activation process. Fig. 4b showed the Nyquist plots of the Co₁-N₄ and Co₁-N_{4-x}C_x. On account of the radius of the Nyquist plots, the charge transfer resistance (R_{ct}) of Co₁-N₄ was the same as that of Co₁-N_{4-x}C_x, suggesting that the electrons were to be transferred to CO₂ with a similar faradaic process for Co₁-N₄ and Co₁-N_{4-x}C_x.

The intrinsic reason for central Co active site with different coordination environment towards CO₂ electrochemical reduction was further investigated. To explore the number of active sites on the Co₁-N₄ and Co₁-N_{4-x}C_x, we investigated the ECSAs. The ECSAs of the two catalysts were calculated by measuring the C_{dl} , derived from the cyclic voltammograms technique under different scan rates in CO₂-saturated 0.1 M KHCO₃ electrolyte (Fig. S16). Fig. 4c showed the charging current density differences plotted against scan rates on Co₁-N₄ and Co₁-N_{4-x}C_x. Obviously, the C_{dl} (5.32 mF cm⁻²) of Co₁-N₄ was close to that (5.95 mF cm⁻²) of the Co₁-N_{4-x}C_x, indicating that the high FE and current density for Co₁-N₄ were independent of the numbers of active

site. Fig. 4d showed CO₂-TPD profiles of the Co₁-N₄ and Co₁-N_{4-x}C_x. The high desorption temperature corresponded to the stronger binding strength between catalyst and adsorbate [46,47]. The chemical desorption peak for Co₁-N₄ and Co₁-N_{4-x}C_x were located at the temperature of 520 °C and 499 °C, respectively, revealing that Co₁-N₄ exhibited the stronger binding strength to CO₂ than that of Co₁-N_{4-x}C_x. In addition, the peak area of TPD profile depended on the adsorption capacity [48]. The CO₂-TPD profiles measurements showed that the Co₁-N₄ had a significantly larger adsorption capacity of CO₂ than that of Co₁-N_{4-x}C_x. After the treatment of CO₂ adsorption at room temperature, the DRIFTS spectra of Co₁-N₄ and Co₁-N_{4-x}C_x was shown in Fig. S17. A characteristic peak at 1344 cm⁻¹ was observed in the spectrum of Co₁-N₄, which was attributed to the stretching vibration of CO₂-. With regard to Co₁-N_{4-x}C_x, the peak associated with the stretching vibration of CO₂- was blue-shifted to 1357 cm⁻¹, indicating that Co₁-N₄ exhibited stronger binding strength with CO₂ than that of Co₁-N_{4-x}C_x. These results further revealed that the enhancement of activity for Co₁-N₄ towards CO₂ electrochemical reduction was mainly attributed to the strong binding strength and large adsorption capacity with CO₂ due to the different coordination environment, rather than the increasing number of active site.

4. Conclusion

In summary, we select ZnCo bimetallic MOF as precursor to assist the preparation of Co single-atom catalysts, where the Co single atom with different coordination environment was regulated by pyrolysis temperature. During CO₂ electrochemical reduction process, the Co₁-N₄ exhibited a FE of 82% and a current density of -15.8 mA cm⁻² for CO production. Mechanistic study further revealed that Co₁-N₄ exhibited the higher catalytic performance than that of Co₁-N_{4-x}C_x originate from the promoted binding strength of CO₂ and the facilitated CO₂ activation, due to the difference of the coordination environment with central Co active site. This work would provide a guideline for the rational design of single-atom catalysts with highly catalytic activity towards CO₂ electrochemical reduction by regulating coordination environment with the active site.

Acknowledgements

This work was supported by National Natural Science Foundation of China (51601186, 11404314, and 21471143) and Natural Science Foundation of Anhui Province (1708085MA06).

Appendix A. Supplementary data

Supplementary material related to this article can be found, in the online version, at doi:<https://doi.org/10.1016/j.apcatb.2018.08.075>.

References

- [1] H. Mistry, Y.-W. Choi, A. Bagger, F. Scholten, C.S. Bonifacio, I. Sinev, N.J. Divins, I. Zegkinoglou, H.S. Jeon, K. Kisslinger, E.A. Stach, J.C. Yang, J. Rossmeisl, B.R. Cuenya, Enhanced carbon dioxide electroreduction to carbon monoxide over defect rich plasma-activated silver catalysts, *Angew. Chem. Int. Ed.* 56 (2017) 11394–11398.
- [2] C.S. Le Duff, M.J. Lawrence, P. Rodriguez, Role of the adsorbed oxygen species in the selective electrochemical reduction of CO₂ to alcohols and carbonyls on copper electrodes, *Angew. Chem. Int. Ed.* 56 (2017) 12919–12924.
- [3] Z. Weng, X. Zhang, Y. Wu, S. Huo, J. Jiang, W. Liu, G. He, Y. Liang, H. Wang, Self-cleaning catalyst electrodes for stabilized CO₂ reduction to hydrocarbons, *Angew. Chem. Int. Ed.* 56 (2017) 13135–13139.
- [4] Y. Mun, K. Kim, S. Kim, S. Lee, S. Kim, W. Choi, S.-K. Kim, J.W. Han, J. Lee, A novel strategy to develop non-noble metal catalyst for CO₂ electroreduction: hybridization of metal-organic polymer, *Appl. Catal. B-Environ.* 236 (2018) 154–161.
- [5] S. Lin, C.S. Diercks, Y.-B. Zhang, N. Kornienko, E.M. Nichols, Y. Zhao, A.R. Paris, D. Kim, P. Yang, O.M. Yaghi, C.J. Chang, Covalent organic frameworks comprising cobalt porphyrins for catalytic CO₂ reduction in water, *Science* 349 (2015) 1208–1213.
- [6] J. Rosen, G.S. Hutchings, Q. Lu, R.V. Forest, A. Moore, F. Jiao, Electrodeposited Zn

- dendrites with enhanced CO selectivity for electrocatalytic CO₂ reduction, *ACS Catal.* 5 (2015) 4586–4591.
- [7] T. Zhang, X. Li, Y. Qiu, P. Su, W. Xu, H. Zhong, H. Zhang, Multilayered Zn nanosheets as an electrocatalyst for efficient electrochemical reduction of CO₂, *J. Catal.* 357 (2018) 154–162.
- [8] S. Zhao, Z. Tang, S. Guo, M. Han, C. Zhu, Y. Zhou, L. Bai, J. Gao, H. Huang, Y. Li, Y. Liu, Z. Kang, Enhanced activity for CO₂ electroreduction on a highly active and stable ternary Au-CDots-C₃N₄ electrocatalyst, *ACS Catal.* 8 (2017) 188–197.
- [9] M. Liu, Y. Pang, B. Zhang, P. De Luna, O. Voznyy, J. Xu, X. Zheng, C.T. Dinh, F. Fan, C. Cao, P.P.G. de Arquer, T.S. Safaei, A. Mepham, A. Klinkova, E. Kumacheva, T. Filleter, D. Sinton, S.O. Kelley, E.H. Sargent, Enhanced electrocatalytic CO₂ reduction via field-induced reagent concentration, *Nature* 537 (2016) 382–386.
- [10] D. Gao, H. Zhou, J. Wang, S. Miao, F. Yang, G. Wang, J. Wang, X. Bao, Size-dependent electrocatalytic reduction of CO₂ over Pd nanoparticles, *J. Am. Chem. Soc.* 137 (2015) 4288–4291.
- [11] H. Song, M. Im, J.T. Song, J.-A. Lim, B.-S. Kim, Y. Kwon, S. Ryu, J. Oh, Effect of mass transfer and kinetics in ordered Cu-mesoporous structures for electrochemical CO₂ reduction, *Appl. Catal. B-Environ.* 232 (2018) 391–396.
- [12] S. Zhang, P. Kang, M. Bakir, A.M. Lapides, C.J. Dares, T.J. Meyer, Polymer-supported CuPd nanoalloy as a synergistic catalyst for electrocatalytic reduction of carbon dioxide to methane, *Proc. Natl. Acad. Sci.* 112 (2015) 15809–15814.
- [13] M. Dunwell, Q. Lu, J.M. Heyes, J. Rosen, J.G. Chen, Y. Yan, F. Jiao, B. Xu, The central role of bicarbonate in the electrochemical reduction of carbon dioxide on gold, *J. Am. Chem. Soc.* 139 (2017) 3774–3783.
- [14] A. Aljabour, H. Coskun, D.H. Apaydin, F. Ozel, A.W. Hassel, P. Stadler, N.S. Sariciftci, M. Kus, Nanofibrous cobalt oxide for electrocatalysis of CO₂ reduction to carbon monoxide and formate in an acetonitrile-water electrolyte solution, *Appl. Catal. B-Environ.* 229 (2018) 163–170.
- [15] J.-H. Kim, H. Woo, S.-W. Yun, H.-W. Jung, S. Back, Y. Jung, Y.-T. Kim, Highly active and selective Au thin layer on Cu polycrystalline surface prepared by galvanic displacement for the electrochemical reduction of CO₂ to CO, *Appl. Catal. B-Environ.* 213 (2017) 211–215.
- [16] X. Bai, W. Chen, C. Zhao, S. Li, Y. Song, R. Ge, W. Wei, Y. Sun, Exclusive formation of formic acid from CO₂ electroreduction by tunable Pd-Sn alloy, *Angew. Chem. Int. Ed.* 56 (2017) 12219–12223.
- [17] Z. Geng, X. Kong, W. Chen, H. Su, Y. Liu, F. Cai, G. Wang, J. Zeng, Oxygen vacancies in ZnO nanosheets enhance CO₂ electrochemical reduction into CO, *Angew. Chem. Int. Ed.* 57 (2018) 6054–6059.
- [18] Y. Jiao, Y. Zheng, P. Chen, M. Jaroniec, S.-Z. Qiao, Molecular scaffolding strategy with synergistic active centers to facilitate electrocatalytic CO₂ reduction to hydrocarbon/alcohol, *J. Am. Chem. Soc.* 139 (2017) 18093–18100.
- [19] D. Kim, J. Resasco, Y. Yu, A.M. Asiri, P. Yang, Synergistic geometric and electronic effects for electrochemical reduction of carbon dioxide using gold-copper bimetallic nanoparticles, *Nat. Commun.* 5 (2014) 4948.
- [20] C. Zhao, X. Dai, T. Yao, W. Chen, X. Wang, J. Wang, J. Yang, S. Wei, Y. Wu, Y. Li, Ionic exchange of metal-organic frameworks to access single nickel sites for efficient electroreduction of CO₂, *J. Am. Chem. Soc.* 139 (2017) 8078–8081.
- [21] W. Li, B. Herkt, M. Sereydy, T.J. Bandosz, Pyridinic-N groups and ultramicro-pore nanoreactors enhance CO₂ electrochemical reduction on porous carbon catalysts, *Appl. Catal. B-Environ.* 207 (2017) 185–206.
- [22] J. Liu, M. Jiao, L. Lu, H.M. Barkholtz, Y. Li, Y. Wang, L. Jiang, Z. Wu, D.-j. Liu, L. Zhuang, C. Ma, J. Zeng, B. Zhang, D. Su, P. Song, W. Xing, W. Xu, Y. Wang, Z. Jiang, G. Sun, High performance platinum single atom electrocatalyst for oxygen reduction reaction, *Nat. Commun.* 8 (2017) 15938.
- [23] Y.S. Ham, S. Choe, M.J. Kim, T. Lim, S.-K. Kim, J.J. Kim, Electrodeposited Ag catalysts for the electrochemical reduction of CO₂ to CO, *Appl. Catal. B-Environ.* 208 (2017) 35–43.
- [24] C. Cui, J. Han, X. Zhu, X. Liu, H. Wang, D. Mei, Q. Ge, Promotional effect of surface hydroxyls on electrochemical reduction of CO₂ over SnO₂/Sn electrode, *J. Catal.* 343 (2016) 257–265.
- [25] H.-J. Qiu, Y. Ito, W. Cong, Y. Tan, P. Liu, A. Hirata, T. Fujita, Z. Tang, M. Chen, Nanoporous graphene with single-atom nickel dopants: an efficient and stable catalyst for electrochemical hydrogen production, *Angew. Chem. Int. Ed.* 54 (2015) 14031–14035.
- [26] X. Zhang, J. Guo, P. Guan, C. Liu, H. Huang, F. Xue, X. Dong, S.J. Pennycook, M.F. Chisholm, Catalytically active single-atom niobium in graphitic layers, *Nat. Commun.* 4 (2013) 1924.
- [27] B. Qiao, A. Wang, X. Yang, L.F. Allard, Z. Jiang, Y. Cui, J. Liu, J. Li, T. Zhang, Single-atom catalysis of CO oxidation using Pt₁/FeO_x, *Nat. Chem.* 3 (2011) 634–641.
- [28] W. Liu, L. Zhang, W. Yan, X. Liu, X. Yang, S. Miao, W. Wang, A. Wang, T. Zhang, Single-atom dispersed Co-N-C catalyst: structure identification and performance for hydrogenative coupling of nitroarenes, *Chem. Sci.* 9 (2016) 5758–5764.
- [29] H. Fei, J. Dong, M.J. Arellano-Jime'nez, G. Ye, N.D. Kim, E.L.G. Samuel, Z. Peng, Z. Zhu, F. Qin, J. Bao, M.J. Yacaman, P.M. Ajayan, D. Chen, J.M. Tour, Atomic cobalt on nitrogen-doped graphene for hydrogen generation, *Nat. Commun.* 6 (2015) 8668.
- [30] P. Chen, T. Zhou, L. Xing, K. Xu, Y. Tong, H. Xie, L. Zhang, W. Yan, W. Chu, C. Wu, Y. Xie, Atomically dispersed iron-nitrogen species as electrocatalysts for bifunctional oxygen evolution and reduction reactions, *Angew. Chem. Int. Ed.* 56 (2017) 610–614.
- [31] S. Back, J. Lim, N.-Y. Kim, Y.-H. Kim, Y. Jung, Single-atom catalysts for CO₂ electroreduction with significant activity and selectivity improvements, *Chem. Sci.* 8 (2017) 1090–1096.
- [32] X.-F. Li, Q.-K. Li, J. Cheng, L. Liu, Q. Yan, Y. Wu, X.-H. Zhang, Z.-Y. Wang, Q. Qiu, Y. Luo, Conversion of dinitrogen to ammonia by FeN₃-embedded graphene, *J. Am. Chem. Soc.* 138 (2016) 8706–8709.

- [33] F. Xie, H. Wu, J. Mou, D. Lin, C. Xu, C. Wu, X. Sun, Ni₃N@Ni-Ci nanoarray as a highly active and durable non-noble-metal electrocatalyst for water oxidation at near-neutral pH, *J. Catal.* 356 (2017) 165–172.
- [34] M. Yao, N. Wang, W. Hu, S. Komarneni, Novel hydrothermal electrodeposition to fabricate mesoporous film of Ni_{0.8}Fe_{0.2} nanosheets for high performance oxygen evolution reaction, *Appl. Catal. B-Environ.* 233 (2018) 226–233.
- [35] R. Banerjee, A. Phan, B. Wang, C. Knobler, H. Furukawa, M. O'Keeffe, O.M. Yaghi, High-throughput synthesis of zeolitic imidazolate frameworks and application to CO₂ capture, *Science* 319 (2008) 939–943.
- [36] X.-C. Huang, Y.-Y. Lin, J.-P. Zhang, X.-M. Chen, Ligand-directed strategy for zeolite-type metal-organic frameworks: zinc (II) imidazoles with unusual zeolitic topologies, *Angew. Chem. Int. Ed.* 45 (2006) 1557–1559.
- [37] H. Funke, A.C. Scheinost, Wavelet analysis of extended X-ray absorption fine structure data, *Phys. Rev. B* 71 (2005) 094110.
- [38] F. Tuinstra, J.L. Koenig, Raman spectrum of graphite, *J. Chem. Phys.* 53 (1970) 1126–1130.
- [39] S. Wang, L. Zhang, Z. Xia, A. Roy, D.W. Chang, J.-B. Baek, L. Dai, BCN graphene as efficient metal-free electrocatalyst for the oxygen reduction reaction, *Angew. Chem. Int. Ed.* 51 (2012) 4209–4212.
- [40] X. Zhong, Y. Jiang, X. Chen, L. Wang, G. Zhuang, X. Li, J.-G. Wang, Integrating cobalt phosphide and cobalt nitride-embedded nitrogen-rich nanocarbons: high-performance bifunctional electrocatalysts for oxygen reduction and evolution, *J. Mater. Chem. A* 4 (2016) 10575–10584.
- [41] X. Zhong, L. Liu, Y. Jiang, X. Wang, L. Wang, G. Zhuang, X. Li, D. Mei, J.-G. Wang, D.S. Su, Synergistic effect of nitrogen in cobalt nitride and nitrogen-doped hollow carbon spheres for the oxygen reduction reaction, *ChemCatChem* 7 (2015) 1826–1832.
- [42] W. Zhu, R. Michalsky, O. Metin, H. Lv, S. Guo, C.J. Wright, X. Sun, A.A. Peterson, S. Sun, Monodisperse Au nanoparticles for selective electrocatalytic reduction of CO₂ to CO, *J. Am. Chem. Soc.* 135 (2013) 16833–16836.
- [43] D.H. Won, H. Shin, J. Koh, J. Chung, H.S. Lee, H. Kim, S.I. Woo, Highly efficient, selective, and stable CO₂ electroreduction on a hexagonal Zn catalyst, *Angew. Chem. Int. Ed.* 55 (2016) 9297–9300.
- [44] S. Liu, H. Tao, L. Zeng, Q. Liu, Z. Xu, Q. Liu, J.-L. Luo, Shape-dependent electrocatalytic reduction of CO₂ to CO on triangular silver nanoplates, *J. Am. Chem. Soc.* 139 (2017) 2160–2163.
- [45] Y. Chen, C.W. Li, M.W. Kanan, Aqueous CO₂ reduction at very low overpotential on oxide-derived Au nanoparticles, *J. Am. Chem. Soc.* 134 (2012) 19969–19972.
- [46] W. Guo, D.G. Vlachos, Patched bimetallic surfaces are active catalysts for ammonia decomposition, *Nat. Commun.* 6 (2015) 8619.
- [47] Q. Li, W. Xie, G. Chen, Y. Li, Y. Huang, X. Chen, The behaviors of ultra-low-gold-loaded catalysts (Au/CeO₂) for CO oxidation in the presence of water on the catalysts, *Nano Res.* 8 (2015) 3075–3084.
- [48] D. Deng, X. Chen, L. Yu, X. Wu, Q. Liu, Y. Liu, H. Yang, H. Tian, Y. Hu, P. Du, R. Si, J. Wang, X. Cui, H. Li, J. Xiao, T. Xu, J. Deng, F. Yang, P.N. Duchesne, P. Zhang, J. Zhou, L. Sun, J. Li, X. Pan, X. Bao, A single iron site confined in a graphene matrix for the catalytic oxidation of benzene at room temperature, *Sci. Adv.* 1 (2015) e1500462.